## Heterogeneous impacts of fire-sourced ozone (O<sub>3</sub>) pollution on global

	• 11	•	41 C 4	1.	•
cron	vields	ın	the future	climate	scenarios
CIUP	yicius	111	uic iutuic	CIIIIIatt	occiiai ios

- 3 Rui Li<sup>a, b</sup>, Yumeng Shao<sup>a</sup>, Dongmei Tang<sup>a, b, \*</sup>, Yining Gao<sup>a</sup>, Hongfang Zhao<sup>a \*</sup>
- 4 a Key Laboratory of Geographic Information Science of the Ministry of Education, School of
- 5 Geographic Sciences, East China Normal University, Shanghai, 200241, PR China
- 6 b Institute of Eco-Chongming (IEC), 20 Cuiniao Road, Chenjia Town, Chongming District,
- 7 Shanghai, 202162, China
- 8 \* Corresponding author
- 9 Prof. Tang (dmtang@geo.ecnu.edu.cn) and Prof. Zhao (hfzhao@geo.ecnu.edu.cn)
- 10 Abstract

1

2

- 11 Wildfire smoke often aggravates the ozone (O<sub>3</sub>) pollution and negatively affect crop yields. To date,
- 12 the global impact of fire-sourced O<sub>3</sub> exposure on crop yields still remained unknown. To address
- 13 this issue, a multi-stage model was developed to quantify the global wildfire-induced ambient O<sub>3</sub>
- 14 concentrations in the future scenarios. The results suggested that the relationship between observed
- 15 K<sup>+</sup> and levoglucosan levels with simulated fire-sourced maximum daily average 8-hour (MDA8) O<sub>3</sub>
- concentration reached 0.67 and 0.73, respectively, indicating the robustness of fire-sourced O<sub>3</sub>
- estimate. In both of historical and future scenarios, Sub-Sahara Africa (SS:  $14.9 \pm 8.4$  (historical)
- and  $18.3 \pm 9.6$  (mean of the future scenarios)  $\mu g/m^3$ ) and South America (SA:  $4.0 \pm 2.5$  and  $4.7 \pm 1.0$
- 19 3.2  $\mu$ g/m<sup>3</sup>) showed the highest fire-sourced MDA8 O<sub>3</sub> concentrations among all of the regions.
- 20 However, the crop production losses (CPL) caused by O<sub>3</sub> exposure reached the highest values in
- 21 China due to very high total crop yields and relatively high wildfire-induced MDA8 O<sub>3</sub> levels.
- 22 Moreover, CPL in China was sensitive to emission scenario, indicating the effective emission
- 23 control could largely decrease fire-sourced O<sub>3</sub> damage to crop. In contrast, both of SS and SA even
- 24 showed the higher CPL in low-carbon scenario (SSP1-2.6), suggesting more stringent control
- 25 measures are required to offset the wildfire contribution. Our findings call for attention on the threat
- 26 to future global food security from the absence of pollution mitigation and the persistence of global
- 27 warming
- 28 Keywords: MDA8 O<sub>3</sub>, wildfire, crop yield, Sub-Sahara Africa, China
- 29 1. Introduction

Along with the warming climate, large-scale wildfire events have experienced dramatic increases in frequency and intensity in the past decades, and the wildfire seasons have been significantly prolonged in many regions such as the western part of the United States and Australia (Jones et al. 2022, Richardson et al. 2022, Wang et al. 2022). Wildfire often released a large number of gaseous precursors such as carbon monoxide (CO), nitrogen dioxides (NO<sub>x</sub>), and volatile organic compounds (VOC) (Anderson et al. 2024, Xu et al. 2022), which could significantly enhance the ozone (O<sub>3</sub>) levels through photochemical reactions (Jaffe et al. 2013). Recent studies have revealed that wildfire contributed to 3.6% of ambient all-source O<sub>3</sub> level globally (Xu et al. 2023). The aggravation of O<sub>3</sub> pollution not only poses detrimental effects on human health (Liu et al. 2018), but also reduced the crop yields because the excessive O<sub>3</sub> exposure could affect plant photosynthesis via stomatal uptake (Karmakar et al. 2022, Zhao et al. 2020). Thus, quantifying the negative impacts of fire-sourced O<sub>3</sub> pollution on crop yields was beneficial to propose optimal strategy to ensure agricultural production.

Notably, warming climate in the future not only would increase wildfire burned areas, but also intensified the severity of fire weather (Richardson et al. 2022, Wasserman and Mueller 2023). Moreover, wildfire and heatwave have generated the positive feedback and the mechanism would be further enhanced in the future (Senande-Rivera et al. 2022, Zhao et al. 2024). Meanwhile, the ambient O<sub>3</sub> concentration was very sensitive to air temperature, and the continuous increase of air temperature inevitably aggravate wildfire-related O<sub>3</sub> pollution in the future (Bloomer et al. 2009, Li et al. 2024a, Selin et al. 2009). Therefore, it is necessary to analyze the spatiotemporal characteristics of global wildfire-induced O<sub>3</sub> concentrations especially in the future scenarios, which was favorable to accurately identify the hotspots for wildfire-induced O<sub>3</sub> pollution and to propose effective control measures targeting different future scenarios.

A growing body of studies have focused on the wildfire contribution to  $O_3$  pollution. Lee et al. (2024) employed the generalized additive model (GAM) to predict the wildfire-related  $O_3$  concentration in the United States and found wildfire increased maximum daily average 8-hour (MDA8)  $O_3$  concentration across the entire country (Lee and Jaffe 2024). Besides, Xu et al. (2023) have quantified that the wildfire led to average  $3.2 \,\mu\text{g/m}^3$  increase of  $O_3$  concentration globally using the GEOS-Chem model. Unfortunately, most of the current studies assessed the contribution

of historical wildfire to ambient O<sub>3</sub> level, and the estimates showed large uncertainties associated with the burned areas, fuel consumption, and fuel types. Moreover, most of these studies only focused on the historical estimates, while only two studies explored the wildfire contribution to O<sub>3</sub> pollution in the future scenarios (Yang et al. 2022, Yue et al. 2015). Both of these studies only focused on wildfire in North America, whereas the future wildfire contribution to O<sub>3</sub> pollution in other regions are still unknown. Moreover, their negative impacts on crop yields are also not clear. In fact, the global wheat yield losses reached 0.95% (around 20 t/km²) per ppb O<sub>3</sub> increase (Guarin et al. 2019). Although the current contribution ratio of wildfire to all-source O<sub>3</sub> level is not high, the higher wildfire risk and total crop yields in the future scenarios highlights the seriousness of crop yield losses.

Here, our study developed an ensemble machine-learning model to predict fire-sourced MDA8 O<sub>3</sub> levels under four future scenarios (SSP1-2.6, SSP2-4.5, SSP3-7.0, and SSP5-8.5). Then, the spatiotemporal variations of these concentrations and the key drivers behind them were further revealed. Finally, a crop yield loss assessment framework was applied to quantify the negative impacts (crop yield losses) of wildfire-induced O<sub>3</sub> exposure on global crop yield. The hotspots of crop yield losses in different scenarios should be determined and the appropriate control measures should be proposed to reduce the economic losses.

## 2. Materials and methods

# 2.1 Data preparation

Most ground-level MDA8 O<sub>3</sub> observations focused on East Asia, India, Western Europe, and the contiguous United States. Daily MDA8 O<sub>3</sub> data during 2015-2019 over China were collected from the Ministry of Ecology and Environment of China. The observation network comprises of 2,000 monitoring sites distributed across various land-use types (Figure S1). Quality assurance for the ground-level observations in China was performed based on the HJ 630-2011 specifications. The dataset of daily MDA8 O<sub>3</sub> concentrations from 2015 to 2019 in India were collected from the Central Pollution Control Board (CPCB) online database (<a href="https://app.cpcbccr.com/ccr/#/caaqm-dashboard-all/caaqm-landing">https://app.cpcbccr.com/ccr/#/caaqm-dashboard-all/caaqm-landing</a>). The detailed data quality assurance/control has been introduced by Gurjar et al. (2016). Ground-level observation dataset for member countries of the European Economic Area were collected from the European Environment Agency. The data quality control of

European Environment Agency was explained by Keller et al. (2021). The dataset of daily MDA8 O<sub>3</sub> levels in more than 200 monitoring sites across the United States were downloaded from the website of https://www.epa.gov/ (Figure S1). The quality control of these observations in EPA was carefully introduced by (Lamsal et al. 2015). Observation data in other countries and territories were downloaded from the website of OpenAQ (https://openaq.org/). After the data cleaning and quality control, more than 300,000 daily MDA8 O<sub>3</sub> measurements in 3015 sites were collected to simulate the global O<sub>3</sub> concentrations. For O<sub>3</sub>, 1 part per billion (ppb) was approximated as 1.96 μg/m³ based on the standard air pressure and temperature (25.5 °C and 101.325 kPa). The Unite of O<sub>3</sub> was changed into μg/m³ unified.

88 89

90

91 92

93 94

95

96

97

98

99

100

101102

103104

105

106

107

108109

110

111

112

113

114

115

116

GEOS-Chem (v13.4.0) model was utilized to estimate atmospheric MDA8 O3 concentrations during Jan. 1-Dec. 31 during 2015-2019, 2045-2049, and 2095-2099 periods. In our study, the years of 2015-2019 was regarded as the historical period, whereas the years of 2045-2049 and 2095-2099 were regarded as the future period. This model comprises of a complex chemistry mechanism of tropospheric NO<sub>x</sub>-VOC-O<sub>3</sub>-aerosol (Geddes et al. 2015, Zhao et al. 2017). This model for O<sub>3</sub> estimates during historical period and future scenario were driven by MERRA2 and GCAP2 CMIP6 reanalysis meteorological factors, respectively (Bali et al. 2021, Zhang 2016). The future scenario includes SSP1-2.6 (low-carbon emission scenario), SSP2-4.5 (middle-carbon emission scenario), SSP3-7.0 (traditional energy scenario), and SS5-8.5 (high energy consumption scenario). A global simulation was performed at a spatial resolution of 2 × 2.5° resolution (Bindle et al. 2021, Wainwright et al. 2012). The historical anthropogenic emission inventory during 2015-2019 was downloaded from Community Emissions Data System (CEDS) (Hoesly et al. 2018). The anthropogenic and wildfire emissions during 2045-2049 and 2095-2099 were collected from the website of https://esgf-node.llnl.gov/search/input4mips/. Wildfire emission during 2015-2019 was obtained from GFED (Chen et al. 2023, Pan et al. 2020, Peiro et al. 2022, van Wees et al. 2022). Some other natural emission such as the lightning NO<sub>x</sub> emission was collected from http://geoschemdata.wustl.edu/ExtData/HEMCO/OFFLINE\_LIGHTNING/v2020-03/MERRA2/ (Li et al. 2022, Nault et al. 2017, Verma et al. 2021). The whole simulation processes included four steps. Firstly, we run the GEOS-Chem model with all emissions (including wildfires) to establish reference O<sub>3</sub> concentrations (Baseline simulation). Second, we repeated the simulation while

excluding wildfire emissions with the same meteorological conditions (MERRA2 and GCAP2\_CMIP6) and anthropogenic emission inventory (CEDS). Third, we computed the wildfire-induced O<sub>3</sub> by subtracting zero-out results from the baseline. At last, we compare modeled O<sub>3</sub> concentrations with observational data (e.g., ground-based measurements) to assess uncertainty.

Meteorological factors including 2 m dewpoint temperature (D2m), surface pressure (Sp), 2 m temperature (T2m), and total precipitation (Tp), 10 m wind component (U10 and V10) during 2015-2019 were collected from the fifth-generation European Centre for Medium-Range Weather Forecasts Reanalysis (ERA-5). All of these meteorological data showed the same spatial resolution of 0.25°×0.25°. For the estimates in the future scenarios, the CMIP6 dataset in four scenarios (e.g., SSP1-2.6, SSP2-4.5, SSP3-7.0, and SSP5-8.5) were also applied to predict MDA8 O<sub>3</sub> concentrations during 2015-2019, 2045-2049, and 2095-2099. The dataset includes simulated O<sub>3</sub> concentrations, 2-m air temperatures, wind speed at 850 and 500 hPa, total cloud cover, precipitation, relative humidity, and short-wave radiation. The modelled meteorological parameters and chemical compositions derived from multiple earth system models were integrated into the machine-learning model. The detailed models are introduced in our previous studies (Li et al. 2024b). The elevation was collected from ETOPO at a spatial resolution of 1°. Additionally, the land use type data were downloaded from the reference of Liu et al. (2020).

## 2.2 Model development

A multi-stage model was developed to estimate the global fire-sourced MDA8 O<sub>3</sub> concentrations (Figure S2). In the first stage, the ground-level MDA8 O<sub>3</sub> levels, meteorological factors, land use types, and simulated O<sub>3</sub> levels derived from GEOS-Chem model were integrated into XGBoost model to simulate the full-coverage MDA8 O<sub>3</sub> levels during 2015-2019. In the second stage, the simulated O<sub>3</sub> concentrations and meteorological parameters in four scenarios (SSP1-2.6, SSP2-4.5, SSP3-7.0, and SSP5-8.5) during 2015-2019, 2045-2049, and 2095-2099 were collected from CMIP6 dataset including 16 earth system models. Then, the data in the future scenarios were integrated into the XGBoost model to further calibrate the CMIP6 modeling results based on historical dataset (2015-2019) derived from the first stage model. This stage could obtain the calibrated MDA8 O<sub>3</sub> concentrations in different scenarios during 2015-2019, 2045-2049, and 2095-2099. The detailed equations of XGBoost model are summarized as follows:

 $F^{(t)} = \sum_{i=1}^{n} [l(y_{i}, y^{\Lambda^{(t-1)}}) + \partial_{y^{(t-1)}} l(y_{i}, y^{\Lambda^{(t-1)}}) f_{t}(x_{i}) + \frac{1}{2} \partial_{y^{(t-1)}}^{2} l(y_{i}, y^{\Lambda^{(t-1)}}) f_{t}^{2}(x_{i})] + \Omega(f_{t})$   $\tag{1}$ 

where  $F^{(t)}$  represents the cost function at the t-th period;  $\partial$  denotes the derivative of the function;

148  $\partial_{-(t-1)}^2$  means the second derivative of the function; *l* refers to the differentiable convex loss function

that reveals the difference of the predicted  $O_3$  level (y) of the i-th instance at the t-th period and

the target value (y<sub>i</sub>);  $f_t(x)$  is the increment;  $\Omega(f_t)$  reflects the regularizer. Maximum tree depth

and learning rate are 20 and 0.1, respectively.

146

149

150

152

153154

155

156

157

158

159

160

161

162

163

164

165

166

167

168

171

All of the independent variables obtained from various sources were resampled to 0.25° grids using Kriging interpolation. For the machine-learning model development, it was necessary to eliminate some redundant independent variables and then determine the optimal variable group. The redundant variables were identified based on the fact that the overall predictive accuracy could degrade after the removal of these variables. 10-fold cross-validation method was applied to examine the predictive accuracy of XGBoost model.

In the third/final stage, the calibrated MDA8 O<sub>3</sub> concentrations based on previous two-stage models were utilized to optimize the fire-sourced MDA8 O<sub>3</sub> concentrations. Due to uncertainties in the GFED and anthropogenic emission inventories, as well as in the chemical mechanisms, the simulated total and fire-sourced MDA8 O<sub>3</sub> concentrations often deviate substantially from ground-based observations. Therefore, it is essential to use the calibrated MDA8 O<sub>3</sub> concentrations from the previous two stages rather than the originally simulated values to adjust the fire-sourced O<sub>3</sub> levels. However, the magnitude of the error between the simulated fire-sourced O<sub>3</sub> concentrations and the actual values cannot be directly quantified. Based on previous studies (McDuffie et al., 2021), we assumed that the ratio of simulated fire-sourced O<sub>3</sub> concentration to simulated total O<sub>3</sub> concentration from the GEOS-Chem model was equivalent to the ratio of optimized fire-sourced O<sub>3</sub>

$$O_{3\_opt\_fire} = O_{3\_cal\_total} \times (O_{3\_chem\_fire} / O_{3\_chem\_total})$$
(2)

where  $O_{3 \text{ opt fire}}$  is optimized wildfire-induced MDA8  $O_{3}$  concentration in the final stage.

 $O_{3\_cal\_total}$  is calibrated total MDA8  $O_{3}$  concentration.  $O_{3\_chem\_fire}$  is simulated wildfire-induced

concentration to calibrated total O3 concentration. The detailed equations are summarized as follows:

**设置了格式:** 下标

设置了格式: 下标

设置了格式: 下标

**设置了格式:** 下标

**设置了格式:** 下标

MDA8  $O_3$  concentration using GEOS-Chem model.  $O_{3\_chem\_total}$  is simulated total MDA8  $O_3$  concentrations using GEOS-Chem model.

In future simulations of fire-sourced MDA8 O<sub>3</sub> concentrations, we did not apply the historical ratio of fire-sourced O<sub>3</sub> to total O<sub>3</sub> concentrations to future scenarios directly, but used the GEOS-Chem model to calculate the ratios of fire-sourced O<sub>3</sub> to total O<sub>3</sub> concentrations under four future climate scenarios.

The modelling accuracy of wildfire emission to fire-induced MDA8 O<sub>3</sub> cannot be evaluated directly, whereas the modelling performance of total MDA8 O<sub>3</sub> concentrations could be assessed. Some typical statistical indices (supporting information) were applied to evaluate the modelling accuracy of this model on the basis of the ground-level observations. For the accuracy of fire-sourced MDA8 O<sub>3</sub> estimate, we used some fire fingerprints (K<sub>2</sub><sup>+</sup> and levoglucosan) to assess their relationships with fire-sourced O<sub>3</sub> concentrations. This method could also examine whether the assumption of in the stage 3 was right and suitable to our study.

2.3 The crop yield loss estimate

Maize, rice, spring wheat, and winter wheat were major food crops globally, and they were sensitive to O<sub>3</sub> stress. A typical AOT40 exposure index was defined to assess the negative impact of O<sub>3</sub> exposure on crop yields. The AOT40 index was calculated by summing the hourly mean O<sub>3</sub> levels above 40 ppb during the 8 h over the crop growing season.

$$AOT_{40}(ppbh) = \sum_{i=1}^{n} ([CO_3] - 40) [CO_3] \ge 40 \text{ ppb } (3)$$

where [CO<sub>3</sub>]<sub>i</sub> is the hourly O<sub>3</sub> (ppb), and n denotes the number of hours over the growing season. This growing season was determined by the University of Wisconsin Center for Sustainability and the Global Environment (UW SAGE) global crop calendar containing the planting and harvest dates by crop species and variety (Sacks et al., 2010; Schiferl et al., 2018). To date, some OTC/FACE experiments have been applied to assess the adverse effects of elevated O<sub>3</sub> concentrations on maize, rice, spring wheat, and winter wheat. The relationships between AOT40 and the relative yields (RY) for major crops have also been developed in recent years. The detailed equations are shown in Table S1. The relative yield loss (RYL) of crop is defined as

RYL=1-RY (4)

设置了格式: 下标<br/>带格式的: 缩进: 首行缩进: 2字符<br/>设置了格式: 下标<br/>设置了格式: 下标<br/>设置了格式: 下标<br/>设置了格式: 下标

**设置了格式:** 下标 **设置了格式:** 上标 设置**了格式:** 下标 The estimated yield and economic losses are not only related to the RYL, while also associated with the grain yield in each grid. The detail equations are shown as follows:

$$CPL_{i} = RYL_{i} \times CP_{i} / (1 - RYL_{i})$$
 (5)

where  $CPL_i$  is the estimated crop production loss and  $CP_i$  is the actual crop production in each grid during the study period.

The data about actual crop production in each grid were collected from The Agricultural Model Intercomparison and Improvement Project (AgMIP). The average value of simulated crop yields based on four models including DSSAT-Pythia, pDSSAT, LPJ-GUESS, and LPJ-ML were applied to estimate the actual crop production in each grid during 2015-2019, 2045-2049, and 2095-2099.

We selected the simulate results of these models because they showed the better accuracy.

### 3. Results and discussions

### 3.1 Model evaluation

Multi-source information data were integrated into the multi-stage model to predict fire-sourced MDA8 O<sub>3</sub> concentrations globally. At first, the global MDA8 O<sub>3</sub> simulation was evaluated. As illustrated in Figure S3, the 10-fold cross-validation (CV) results suggested that the R² value for MDA8 O<sub>3</sub> estimate reached 0.72. The root mean square error (RMSE) and mean absolute error (MAE) for MDA8 O<sub>3</sub> were 18.1 and 13.2 μg/m³, respectively (Figure S3). The CV R² value in our study reached 0.72, which was higher than that estimated by Liu et al. (2020) (0.64), indicating the satisfied predictive accuracy of O<sub>3</sub> estimates. However, the result was slightly lower than that (R²: 0.80 and 0.81) estimated by Xu et al. (2023) and Delang et al. (2021). It was supposed that the training samples in our study was much less than those used by Xu et al. (2023) (2000-2019 simulation) and Delang et al. (2021) (1990-2019 simulation). It was well known that the predictive accuracy was strongly dependent on the sample size (Li et al. 2020a, Li et al. 2020b). Overall, the predictive performance of ambient O<sub>3</sub> pollution was robust.

Although the prediction capability of this model has been well validated, the accuracy for the fire-sourced MDA8 O<sub>3</sub> estimates could not be directly tested. It is well-known that potassium (K<sup>+</sup>) is often considered to be a fingerprint of wildfire, and thus we employ the relationship between ground-level K<sup>+</sup> observations and wildfire-induced MDA8 O<sub>3</sub> concentrations to examine the modelling accuracy. As shown in Figure S3, the correlation (R value) between observed K<sup>+</sup> levels

and fire-sourced MDA8  $O_3$  concentrations reached 0.67 (146 training samples), which was above 0.5 (p < 0.01). The results have confirmed that the wildfire-induced  $O_3$  estimate showed the satisfied predictive performance. Although  $K^+$  has been often applied to reflect the wildfire contribution, the  $K^+$  could be also derived from anthropogenic emission and dust resuspension. To further validate the modelling performance of wildfire-related MDA8  $O_3$ , the strong fire fingerprint (levoglucosan) was employed to construct the relationship with fire-sourced MDA8  $O_3$  concentrations. The results suggested that the R value (R = 0.73) was even higher than that between observed  $K^+$  levels and fire-sourced MDA8  $O_3$  concentrations. Overall, the predictive performance was close to some previous studies (Childs et al. 2022, O'Dell et al. 2019, Xu et al. 2023), and thus we could use the result to further perform the data analysis.

### 3.2 Spatiotemporal trends of fire-sourced O<sub>3</sub> concentrations

229

230

231

232

233

234

235

236

237

238239

240

241

242

243

244

245246

247

248

249250

251

252

253

254

255

256

257

Global variations of fire-sourced MDA8 O3 concentrations in historical and future scenarios are shown in Figure 1 and 2. From 2015 to 2019, the fire-sourced MDA8 O3 level was in the order of Sub-Saharan Africa (SS) (14.9  $\pm$  8.4  $\mu g/m^3$ ) > South Asia (SA) (4.0  $\pm$  2.5  $\mu g/m^3$ ) > China (1.6  $\pm$  $0.7 \ \mu g/m^3$ ) > United States (US)  $(1.3 \pm 0.9 \ \mu g/m^3)$  > Europe  $(1.2 \pm 0.4 \ \mu g/m^3)$ . In future scenarios, fire-sourced MDA8 O3 levels display marked spatial variability across different Shared Socioeconomic Pathways (SSPs). MDA8 O3 showed the higher concentrations in some regions such as SS, SA, and US. Among all of the scenarios, fire-sourced O3 levels displayed the highest concentrations in SS. It was assumed that this region possessed extensive burned area (52%) and higher biomass fuel consumption (5200 g C m<sup>-2</sup>) compared with other regions (van Wees et al. 2022). Following SS, SA also exhibited the higher wildfire-related MDA8 O<sub>3</sub> concentrations. The elevated concentrations of fire-sourced O3 levels in SA were closely associated with exceptionally high fuel consumption (8600 g C m<sup>-2</sup>) (Chen et al. 2023, van Wees et al. 2022) though the burned areas were not very high among all of the regions. In addition, it should be noted that many previous studies have confirmed US showed the higher wildfire-induced PM2.5 or other aerosol components compared with many other regions (e.g., East Asia and South America) (Park et al. 2024, Xu et al. 2023). However, it did not show the higher O<sub>3</sub> concentrations in nearly all of the scenarios in our study. It was assumed that the MDA8 O3 concentration exhibited significant latitudinal distribution (decreasing with the increase of latitude) globally. Both of China and Europe showed very low

burned areas (0.2%) and fuel consumption (950 g C  $m^{-2}$ ), and thus the fire-sourced MDA8  $O_3$  concentrations were relatively lower compared with SS and SA.

Besides, the fire-sourced MDA8  $O_3$  levels exhibited significant inter-annual trends and large discrepancy between different scenarios. The global average fire-sourced MDA8  $O_3$  concentrations showed overall increase from 2010s  $(1.3\pm0.7~\mu\text{g/m}^3)$  to 2090s (SSP1-2.6, SSP3-7.0, and SSP5-8.5:  $1.9\pm0.9$ ,  $1.6\pm0.8$ , and  $1.4\pm0.7~\mu\text{g/m}^3$ ) for nearly all of the scenarios. The global average wildfire-related MDA8  $O_3$  concentrations (the average of 2040s and 2090s) followed the order of SSP3-7.0  $(1.6\pm0.9~\mu\text{g/m}^3)$  > SSP5-8.5  $(1.5\pm0.8~\mu\text{g/m}^3)$  > SSP1-2.6  $(1.4\pm0.8~\mu\text{g/m}^3)$ . The highest wildfire-related MDA8  $O_3$  levels in SSP3-7.0 (air temperature: about 1.8°C higher than SSP1-2.6) and SSP5-8.5 (air temperature: about 2.3°C higher than SSP1-2.6) scenarios were contributed by the increased fuel consumption and the warmer condition because  $O_3$  level was more sensitive to air temperature increase (Wang et al. 2021, Wu et al. 2021).

Nevertheless, different regions showed distinct long-term trends. Wildfire-related MDA8 O<sub>3</sub> levels in nearly all of the regions in SSP3-7.0 scenario (air temperature: about 1.1°C higher than historical period) showed remarkable increases compared with the historical period because the warmer condition facilitated the rapid increase of O<sub>3</sub> level (Zhao et al. 2020). For low-carbon scenario (SSP1-2.6), the wildfire-related MDA8 O<sub>3</sub> concentrations in China, Europe, and US showed the relatively lower O<sub>3</sub> levels, whereas SA and SS still increased by 40% and 64%, respectively. The results suggested that the low-carbon pathway cannot effectively reduce the wildfire-induced O<sub>3</sub> pollution in both of SA and SS.

3.3 The crop yield losses caused by O<sub>3</sub> exposures

As shown in Figure 3 and 4, the global crop yield losses caused by fire-sourced O<sub>3</sub> exposure have been quantified based on the equations 3-5. During historical period, the global fire-sourced O<sub>3</sub> caused 3.1 (2.4-3.8), 1.7 (1.5-1.9), 24 (21-27), and 43 (39-47) t/km<sup>2</sup> crop losses for maize, rice, spring wheat, and winter wheat, respectively. Compared with the historical period, CPL values in different future scenarios displayed large discrepancy. In SSP1-2.6 scenario, CPL of maize, rice, spring wheat, and winter wheat associated with fire-sourced O<sub>3</sub> exposure were 1.1 (0.9-1.3), 0.5 (0.4-0.6), 4.6 (4.1-5.4), and 4.6 (3.5-5.2) t/km<sup>2</sup>, respectively (Figure S4-S11). However, CPL for maize (2.1 (1.9-2.3) and 2.4 (2.1-3.0) t/km<sup>2</sup>), rice (1.1 (0.9-1.3) and 1.3 (1.1-1.5) t/km<sup>2</sup>), spring

wheat (557 (486-628) and 184 (154-218) t/km<sup>2</sup>), and winter wheat (258 (208-308) and 19 (14-22) t/km²) caused by fire-sourced O<sub>3</sub> exposure experienced dramatic increases in SSP3-7.0 and SSP5-8.5 scenarios (Figure S4-S11). There are two reasons accounting for the fact. First of all, the wildfire-related O<sub>3</sub> exposures showed marked increase in high-emission scenarios (Yang et al. 2022, Yue et al. 2017). Moreover, the crop yields also displayed substantial increases in both of these scenarios because rapid increase of fertilizer consumption (Brunelle et al. 2015, Randive et al. 2021). In addition, CPL caused by fire-sourced O<sub>3</sub> exposure also suffered significant spatial difference. During the historical period, the total CPL for four major foods caused by fire-sourced O<sub>3</sub> exposure in China, Europe, US, SA, and SS were 1451 (1302-1650), 65 (54-82), 61 (48-70), 56 (52-59), and 404 (372-425) t/km<sup>2</sup>, respectively. In the future scenario (SSP1-2.6, SSP3-7.0, and SSP5-8.5), the total CPL for four major foods caused by fire-sourced O3 exposure in China, Europe, US, SA, and SS were 23 (19-28) (711 (630-802) and 339 (299-375)), 14 (12-16) (684 (596-768) and 32 (28-34)), 11 (8-12) (19 (17-22) and 21 (18-23)), 14 (12-15) (35 (30-39) and 21 (18-24)), 298 (272-320) (160 (145-179) and 745 (641-840) t/km<sup>2</sup>, respectively. In both of historical and future scenarios, SS, SA, and China showed the higher CPL compared with other regions. The higher CPL in SS and SA might be attributable to the higher fire-sourced O3 concentrations and crop yields. The higher CPL in China might be associated with exceptionally high crop yields though the wildfire-induced O<sub>3</sub> level was not very high. For most regions, CPL showed the higher values in high-emission scenarios (SSP3-7.0 and SSP5-8.5). Although SS and SA also showed the higher CPL in high-emission scenarios (SSP5-8.5), the CPL values of SS and SA in SSP1-2.6 scenario were still very high. The results suggested that the low-carbon policy still cannot effectively weaken local agricultural damage of fire-sourced O<sub>3</sub> exposure. 3.4 Implications and limitations

Our study developed a multi-stage machine-learning model based on the multi-source information data to predict the fire-sourced MDA8 O<sub>3</sub> concentrations at the global scale. It is the first study to use the ground-level observations as the constraint to improve the O<sub>3</sub> estimates in the future scenarios. The results confirmed that the model showed the better predictive accuracy and transferability.

314 transferability.

287

288

289

290

291

292

293

294

295

296297

298

299

300 301

302

303

304

305

306

307 308

309

310

311

312

313

315

Our assessment highlighted the severity and scale of the fire-sourced MDA8  $O_3$  level and a

notable increasing trend in the future scenarios. Especially in high-emission scenarios (SSP3-7.0 and SSP5-8.5), the fire-sourced MDA8 O<sub>3</sub> showed the higher concentrations compared with the low-carbon scenario. Therefore, the global mean temperature increase should be limited to 2.0 °C or 1.5 °C above pre-industrial levels. In addition, both of SS and SA showed the highest wildfire-induced MDA8 O<sub>3</sub> concentration compared with other regions, indicating these hotspots should be determined to propose some control measures. For instance, wildfires could be partially controlled via effective evidence-based fire management and appropriate planning (González-Mathiesen and March 2021, Gonzalez-Mathiesen et al. 2021). Some prevention policy should be proposed to reduce agricultural waste incineration and some prescribed fires (Koul et al. 2022, Lange and Gillespie 2023). Some wildlands could be also changed into agricultural or commercial lands to reduce the occurrence frequency of forest wildfire (Mansoor et al. 2022).

Besides, the impacts of fire-sourced O<sub>3</sub> pollution on crop yields were also quantified. The results confirmed China was faced of serious crop production losses, which was even higher than those in SS and SA because the higher crop production and increasing O<sub>3</sub> pollution risk in the future scenarios. Overall, crop yield losses of China showed significantly higher values in high-emission scenario (SSP3-7.0 and SSP5-8.5) compared with low-emission scenario (SSP1-2.6). The results suggested that low-carbon policy not only largely weaken O<sub>3</sub> pollution derived from anthropogenic emission in China, but also decrease wildfire-induced O<sub>3</sub> damages to crop yields effectively. The results also confirm that the carbon neutrality policy implemented in China possess sufficient agricultural benefits. In contrast, crop yield losses of SS and SA in low-carbon scenario still showed very high risks. It requires more stringent control measures to further reduce local anthropogenic emission in order to offset the wildfire-induced O<sub>3</sub> contribution.

It should be noted that our study is still subject to some limitations. Firstly, the future wildfire emission inventory still shows some uncertainties because the accuracy of land use types and burned areas in the future scenarios cannot be examined directly. Furthermore, in the historical estimates, we only used a chemical transport model (GEOS-Chem model) to simulate the fire-sourced O<sub>3</sub> concentrations though the ground-level observations were assimilated. However, only one model could increase the uncertainties because the O<sub>3</sub> background might be overestimated. Second, the chemical transport model used in our study did not account for plume rise, which could overestimate

the contribution of wildfire emissions to O<sub>3</sub> pollution. Third, the ground-level observations of ambient O<sub>3</sub> are unevenly distributed around the world, which could limit the predictive accuracy of O<sub>3</sub> levels especially in some regions (e.g., SS and SA) lack of monitoring sites. In the future, it is highly necessary to add sufficient ground-level O<sub>3</sub> observations to further improve the accuracy of O<sub>3</sub> estimates. Finally, the zero-out method might suffer from some limitations because O<sub>3</sub> chemistry is highly nonlinear. More other methods such as air pollutant tracing method should be applied to quantify the fire-sourced O<sub>3</sub> concentrations combined with zero-out method. In the GEOS-Chem model, wildfire-emitted precursors (e.g., NO<sub>x</sub>, VOCs) could be assigned unique "tags" as separate tracers. These tagged species undergo the same transport, chemistry, and deposition processes as regular emissions but are tracked independently. For ozone (O<sub>3</sub>) attribution, the model calculates the fraction of O<sub>3</sub> produced from wildfire-tagged NO<sub>x</sub>/VOCs oxidation pathways. The tagged O<sub>3</sub> concentrations are then extracted to quantify the wildfire contribution, while accounting for nonlinear chemical interactions (e.g., NO<sub>x</sub> saturation effects). The combination of multiple methods could increase the robustness of fire-sourced O<sub>3</sub> estimates.

## Acknowledgements

- 360 This work was supported by the National Natural Science Foundation of China (grant no.
- 361 U23A2030).

345

346

347

348349

350

351

352

353

354

355

356

357

358 359

- 362 Data availability
- 363 The CMIP6 dataset used in this publication is available at https://esgf-
- 364 node.ipsl.upmc.fr/search/cmip6-ipsl.
- 365 Author contributions
- 366 RL, DT, and HZ designed the study. RL developed the model. DT, YS, YG, and HZ analyzed the
- 367 observations and model data. RL wrote the paper. RL and YS revised the paper.
- 368 Competing interests
- 369 The contact author has declared that none of the authors has any competing interests.

**Figure 1** The multi-year average concentrations of fire-sourced MDA8  $O_3$  (Unit:  $\mu g/m^3$ ) during 2015-2019 (2010s) at the global scale (a). The latitudinal variations of fire-sourced MDA8  $O_3$  levels (Unit:  $\mu g/m^3$ ) (b). The spatial distributions of fire-sourced MDA8  $O_3$  concentrations (Unit:  $\mu g/m^3$ ) during 2015-2019 (2010s) (c). US, SA, and SS represent the United States, South America, and Sub-Sahara Africa, respectively. The difference of fire-sourced MDA8  $O_3$  concentrations in different regions (d).

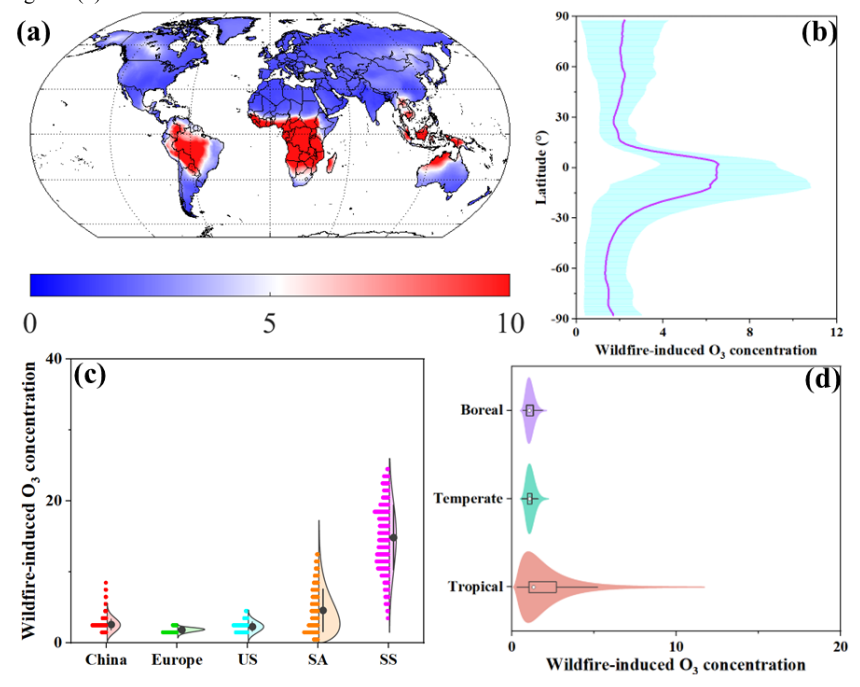


**Figure 2** The global variations of fire-sourced MDA8 O<sub>3</sub> levels (Unit: µg/m³) in SSP1-2.6 (a), SSP3-7.0 (b), and SSP5-8.5 (c) scenarios during 2040s. The spatial distributions of wildfire-related MDA8 O<sub>3</sub> concentrations (Unit: µg/m³) in different regions during 2040s (d). US, SA, and SS represent the United States, South America, and Sub-Sahara Africa, respectively.

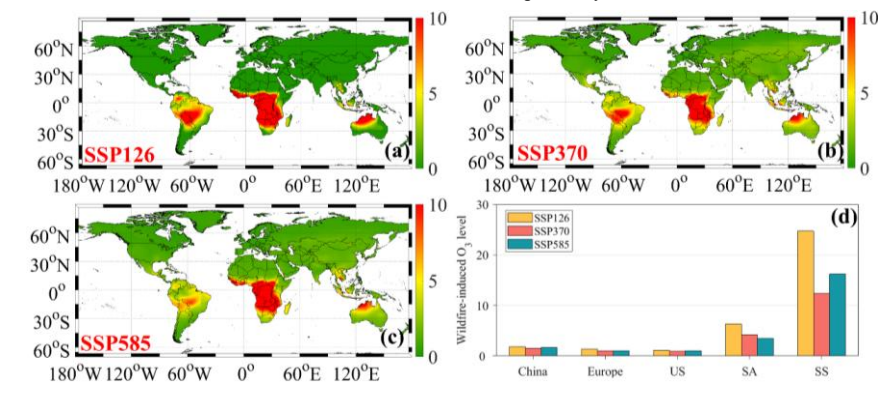


**Figure 3** The global variations of fire-sourced  $O_3$ -related maize yield losses (Unit:  $t/km^2$ ) during historical (a), SSP1-2.6 (b), SSP3-7.0 (d), and SSP5-8.5 (e) scenarios during 2040s, respectively. The spatial variations of fire-sourced maize yield losses (Unit:  $t/km^2$ ) in major regions during 2040s. US, SA, and SS represent the United States, South America, and Sub-Sahara Africa, respectively.

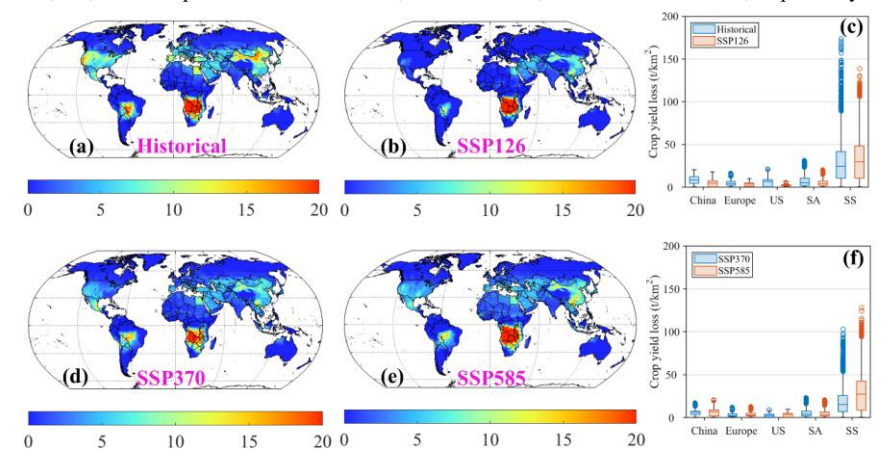
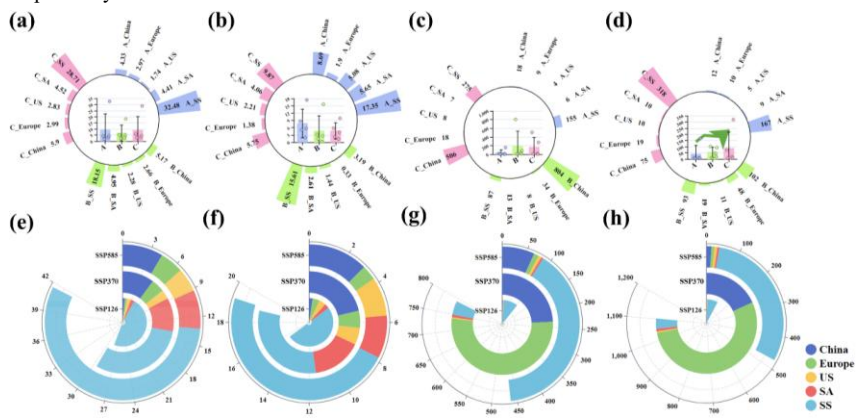


Figure 4 The spatial variations of fire-sourced  $O_3$ -related maize (a), rice (b), spring wheat (c), and winter wheat (d) yield losses (Unit:  $t/km^2$ ) during SSP1-2.6, SSP3-7.0, and SSP5-8.5 scenarios during 2040s, respectively. A, B, and C denote SSP1-2.6, SSP3-7.0, and SSP5-8.5 scenarios, respectively. (e)-(h) represent fire-sourced  $O_3$ -related maize (e), rice (f), spring wheat (g), and winter wheat (h) yield losses during SSP1-2.6, SSP3-7.0, and SSP5-8.5 scenarios during 2090s, respectively. US, SA, and SS represent the United States, South America, and Sub-Sahara Africa, respectively.



#### References

- Anderson, K., Chen, J., Englefield, P., Griffin, D., Makar, P.A. and Thompson, D. (2024) The Global Forest Fire Emissions Prediction System version 1.0. Geoscientific Model Development 17(21), 7713-7749
- Bali, K., Dey, S. and Ganguly, D. (2021) Diurnal patterns in ambient PM2. 5 exposure over India using MERRA-2 reanalysis data. Atmospheric Environment 248, 118180.
- Bindle, L., Martin, R.V., Cooper, M.J., Lundgren, E.W., Eastham, S.D., Auer, B.M., Clune, T.L., Weng, H., Lin, J. and Murray, L.T. (2021) Grid-stretching capability for the GEOS-Chem 13.0. 0 atmospheric chemistry model. Geoscientific Model Development 14(10), 5977-5997.
- Bloomer, B.J., Stehr, J.W., Piety, C.A., Salawitch, R.J. and Dickerson, R.R. (2009) Observed relationships of ozone air pollution with temperature and emissions. Geophysical Research Letters 36(9).
- Brunelle, T., Dumas, P., Souty, F., Dorin, B. and Nadaud, F. (2015) Evaluating the impact of rising fertilizer prices on crop yields. Agricultural economics 46(5), 653-666.
- Chen, Y., Hall, J., van Wees, D., Andela, N., Hantson, S., Giglio, L., van der Werf, G.R., Morton, D.C. and Randerson, J.T. (2023) Multi-decadal trends and variability in burned area from the 5th version of the Global Fire Emissions Database (GFED5). Earth System Science Data Discussions 2023, 1-52
- Childs, M.L., Li, J., Wen, J., Heft-Neal, S., Driscoll, A., Wang, S., Gould, C.F., Qiu, M., Burney, J. and Burke, M. (2022) Daily local-level estimates of ambient wildfire smoke PM2. 5 for the contiguous US. Environmental science & technology 56(19), 13607-13621.
- DeLang, M.N., Becker, J.S., Chang, K.-L., Serre, M.L., Cooper, O.R., Schultz, M.G., Schröder, S., Lu, X., Zhang, L. and Deushi, M. (2021) Mapping yearly fine resolution global surface ozone through the Bayesian maximum entropy data fusion of observations and model output for 1990–2017. Environmental science & technology 55(8), 4389-4398.
- Geddes, J., Heald, C., Silva, S. and Martin, R. (2015) Land cover change impacts on atmospheric chemistry: simulating projected large-scale tree mortality in the United States. Atmospheric Chemistry & Physics Discussions 15(20).
- González-Mathiesen, C. and March, A. (2021) Understanding Disaster Risk, pp. 159-178, Elsevier.
- Gonzalez-Mathiesen, C., Ruane, S. and March, A. (2021) Integrating wildfire risk management and spatial planning—A historical review of two Australian planning systems. International Journal of Disaster Risk Reduction 53, 101984.
- Guarin, J.R., Kassie, B., Mashaheet, A.M., Burkey, K. and Asseng, S. (2019) Modeling the effects of tropospheric ozone on wheat growth and yield. European Journal of Agronomy 105, 13-23.
- Gurjar, B.R., Ravindra, K. and Nagpure, A.S. (2016) Air pollution trends over Indian megacities and their local-to-global implications. Atmospheric Environment 142, 475-495.
- Hoesly, R.M., Smith, S.J., Feng, L., Klimont, Z., Janssens-Maenhout, G., Pitkanen, T., Seibert, J.J., Vu, L., Andres, R.J. and Bolt, R.M. (2018) Historical (1750–2014) anthropogenic emissions of reactive gases and aerosols from the Community Emissions Data System (CEDS). Geoscientific Model Development 11(1), 369-408.
- Jaffe, D.A., Wigder, N., Downey, N., Pfister, G., Boynard, A. and Reid, S.B. (2013) Impact of wildfires on ozone exceptional events in the western US. Environmental science & technology 47(19), 11065-11072.
- Jones, M.W., Abatzoglou, J.T., Veraverbeke, S., Andela, N., Lasslop, G., Forkel, M., Smith, A.J., Burton,

- C., Betts, R.A. and van der Werf, G.R. (2022) Global and regional trends and drivers of fire under climate change. Reviews of Geophysics 60(3), e2020RG000726.
- Karmakar, S.P., Das, A.B., Gurung, C. and Ghosh, C. (2022) Effects of ozone on plant health and environment: A mini review. Res. Jr. Agril. Sci 13, 612-619.
- Keller, C.A., Evans, M.J., Knowland, K.E., Hasenkopf, C.A., Modekurty, S., Lucchesi, R.A., Oda, T., Franca, B.B., Mandarino, F.C. and Díaz Suárez, M.V. (2021) Global impact of COVID-19 restrictions on the surface concentrations of nitrogen dioxide and ozone. Atmospheric Chemistry and Physics 21(5), 3555-3592.
- Koul, B., Yakoob, M. and Shah, M.P. (2022) Agricultural waste management strategies for environmental sustainability. Environmental Research 206, 112285.
- Lamsal, L.N., Duncan, B.N., Yoshida, Y., Krotkov, N.A., Pickering, K.E., Streets, D.G. and Lu, Z. (2015) US NO<sub>2</sub> trends (2005–2013): EPA Air Quality System (AQS) data versus improved observations from the Ozone Monitoring Instrument (OMI). Atmospheric Environment 110, 130-143.
- Lange, J. and Gillespie, J. (2023) Bushfire, prescribed burning, and non-human protection. Geographical Research 61(2), 169-192.
- Lee, H. and Jaffe, D.A. (2024) Wildfire Impacts on O3 in the Continental United States Using PM2. 5 and a Generalized Additive Model (2018–2023). Environmental science & technology 58(33), 14764-14774.
- Li, H., Yang, Y., Su, H., Wang, H., Wang, P. and Liao, H. (2024a) Ozone pollution in China affected by climate change in a carbon neutral future as predicted by a process-based interpretable machine learning method. Geophysical Research Letters 51(13), e2024GL109520.
- Li, M., Mao, J., Chen, S., Bian, J., Bai, Z., Wang, X., Chen, W. and Yu, P. (2022) Significant contribution of lightning NOx to summertime surface O3 on the Tibetan Plateau. Science of the Total Environment 829, 154639.
- Li, R., Cui, L., Fu, H., Meng, Y., Li, J. and Guo, J. (2020a) Estimating high-resolution PM1 concentration from Himawari-8 combining extreme gradient boosting-geographically and temporally weighted regression (XGBoost-GTWR). Atmospheric Environment 229, 117434.
- Li, R., Cui, L., Fu, H., Zhao, Y., Zhou, W. and Chen, J. (2020b) Satellite-Based Estimates of Wet Ammonium (NH<sub>4</sub>-N) Deposition Fluxes Across China during 2011–2016 Using a Space-Time Ensemble Model. Environmental science & technology 54(21), 13419-13428.
- Li, R., Gao, Y., Zhang, L., Shen, Y., Xu, T., Sun, W. and Wang, G. (2024b) Global estimates of ambient reactive nitrogen components during 2000–2100 based on the multi-stage model. Atmospheric Chemistry and Physics 24(13), 7623-7636.
- Liu, H., Liu, S., Xue, B., Lv, Z., Meng, Z., Yang, X., Xue, T., Yu, Q. and He, K. (2018) Ground-level ozone pollution and its health impacts in China. Atmospheric Environment 173, 223-230.
- Liu, R., Ma, Z., Liu, Y., Shao, Y.C., Zhao, W., and Bi, J. (2020) Spatiotemporal distributions of surface ozone levels in China from 2005 to 2017: A machine learning approach. Environment International 142, 105823.
- Mansoor, S., Farooq, I., Kachroo, M.M., Mahmoud, A.E.D., Fawzy, M., Popescu, S.M., Alyemeni, M., Sonne, C., Rinklebe, J. and Ahmad, P. (2022) Elevation in wildfire frequencies with respect to the climate change. Journal of Environmental Management 301, 113769.
- McDuffie, E.E., Martin, R.V., Spadaro, J.V., Burnett, R., Smith, S.J., O'Rourke, P., Hammer, M.S., van Donkelaar, A., Bindle, L., Shah, V. (2021) Source sector and fuel contributions to ambient PM<sub>2.5</sub> and attributable mortality across multiple spatial scales. Nature communications 12, 3594.

- Nault, B., Laughner, J., Wooldridge, P., Crounse, J., Dibb, J., Diskin, G., Peischl, J., Podolske, J., Pollack, I. and Ryerson, T. (2017) Lightning NOx emissions: Reconciling measured and modeled estimates with updated NOx chemistry. Geophysical Research Letters 44(18), 9479-9488.
- O'Dell, K., Ford, B., Fischer, E.V. and Pierce, J.R. (2019) Contribution of wildland-fire smoke to US PM<sub>2.5</sub> and its influence on recent trends. Environmental science & technology 53(4), 1797-1804.
- Pan, X., Ichoku, C., Chin, M., Bian, H., Darmenov, A., Colarco, P., Ellison, L., Kucsera, T., da Silva, A. and Wang, J. (2020) Six global biomass burning emission datasets: intercomparison and application in one global aerosol model. Atmospheric Chemistry and Physics 20(2), 969-994.
- Park, C.Y., Takahashi, K., Fujimori, S., Phung, V.L.H., Li, F., Takakura, J.y., Hasegawa, T. and Jansakoo, T. (2024) Future fire-PM2. 5 mortality varies depending on climate and socioeconomic changes. Environmental Research Letters 19(2), 024003.
- Peiro, H., Crowell, S. and Moore III, B. (2022) Optimizing Four Years of CO 2 Biospheric Fluxes from OCO-2 and in situ data in TM5: Fire Emissions from GFED and Inferred from MOPITT CO data. Atmospheric Chemistry & Physics Discussions.
- Randive, K., Raut, T. and Jawadand, S. (2021) An overview of the global fertilizer trends and India's position in 2020. Mineral Economics, 1-14.
- Richardson, D., Black, A.S., Irving, D., Matear, R.J., Monselesan, D.P., Risbey, J.S., Squire, D.T. and Tozer, C.R. (2022) Global increase in wildfire potential from compound fire weather and drought. NPJ climate and atmospheric science 5(1), 23.
- Sacks, W. J., Deryng, D., Foley, J. A., and Ramankutty, N.: Crop planting dates: an analysis of global patterns, Global Ecol. Biogeogr., 19, 607–620, https://doi.org/10.1111/j.1466-8238.2010.00551.x, 2010.
- Selin, N.E., Wu, S., Nam, K.-M., Reilly, J.M., Paltsev, S., Prinn, R.G. and Webster, M.D. (2009) Global health and economic impacts of future ozone pollution. Environmental Research Letters 4(4), 044014.
- Senande-Rivera, M., Insua-Costa, D. and Miguez-Macho, G. (2022) Spatial and temporal expansion of global wildland fire activity in response to climate change. Nature communications 13(1), 1208.
- van Wees, D., van der Werf, G.R., Randerson, J.T., Rogers, B.M., Chen, Y., Veraverbeke, S., Giglio, L. and Morton, D.C. (2022) Global biomass burning fuel consumption and emissions at 500-m spatial resolution based on the Global Fire Emissions Database (GFED). Geoscientific Model Development Discussions 2022, 1-46.
- Verma, S., Yadava, P.K., Lal, D., Mall, R., Kumar, H. and Payra, S. (2021) Role of lightning NOx in ozone formation: A review. Pure and Applied Geophysics 178, 1425-1443.
- Wainwright, C., Pierce, J., Liggio, J., Strawbridge, K., Macdonald, A. and Leaitch, R. (2012) The effect of model spatial resolution on Secondary Organic Aerosol predictions: a case study at Whistler, BC, Canada. Atmospheric Chemistry and Physics 12(22), 10911-10923.
- Wang, B., Spessa, A.C., Feng, P., Hou, X., Yue, C., Luo, J.-J., Ciais, P., Waters, C., Cowie, A. and Nolan, R.H. (2022) Extreme fire weather is the major driver of severe bushfires in southeast Australia. Science bulletin 67(6), 655-664.
- Wang, Y., Yuan, Q., Li, T., Zhu, L. and Zhang, L. (2021) Estimating daily full-coverage near surface O3, CO, and NO2 concentrations at a high spatial resolution over China based on S5P-TROPOMI and GEOS-FP. ISPRS Journal of Photogrammetry and Remote Sensing 175, 311-325.
- Wasserman, T.N. and Mueller, S.E. (2023) Climate influences on future fire severity: a synthesis of climate-fire interactions and impacts on fire regimes, high-severity fire, and forests in the western

- United States. Fire Ecology 19(1), 1-22.
- Wu, B., Liu, C., Zhang, J., Du, J. and Shi, K. (2021) The multifractal evaluation of PM2. 5-O3 coordinated control capability in China. Ecological Indicators 129, 107877.
- Xu, Q., Westerling, A.L., Notohamiprodjo, A., Wiedinmyer, C., Picotte, J.J., Parks, S.A., Hurteau, M.D., Marlier, M.E., Kolden, C.A. and Sam, J.A. (2022) Wildfire burn severity and emissions inventory: an example implementation over California. Environmental Research Letters 17(8), 085008.
- Xu, R., Ye, T., Yue, X., Yang, Z., Yu, W., Zhang, Y., Bell, M.L., Morawska, L., Yu, P. and Zhang, Y. (2023) Global population exposure to landscape fire air pollution from 2000 to 2019. Nature 621(7979), 521-529.
- Yang, C.-E., Fu, J.S., Liu, Y., Dong, X. and Liu, Y. (2022) Projections of future wildfires impacts on air pollutants and air toxics in a changing climate over the western United States. Environmental pollution 304, 119213.
- Yue, X., Mickley, L., Logan, J., Hudman, R., Martin, M.V. and Yantosca, R. (2015) Impact of 2050 climate change on North American wildfire: consequences for ozone air quality. Atmospheric Chemistry and Physics 15(17), 10033-10055.
- Yue, X., Strada, S., Unger, N. and Wang, A. (2017) Future inhibition of ecosystem productivity by increasing wildfire pollution over boreal North America. Atmospheric Chemistry and Physics 17(22), 13699-13719.
- Zhang, H. (2016) Impacts of global change on tropospheric ozone and mercury, Michigan Technological University.
- Zhao, H., Zheng, Y., Zhang, Y. and Li, T. (2020) Evaluating the effects of surface O3 on three main food crops across China during 2015–2018. Environmental pollution 258, 113794.
- Zhao, J., Yue, C., Wang, J., Hantson, S., Wang, X., He, B., Li, G., Wang, L., Zhao, H. and Luyssaert, S. (2024) Forest fire size amplifies postfire land surface warming. Nature 633(8031), 828-834.
- Zhao, Y., Zhang, L., Tai, A.P., Chen, Y. and Pan, Y. (2017) Responses of surface ozone air quality to anthropogenic nitrogen deposition in the Northern Hemisphere. Atmospheric Chemistry and Physics 17(16), 9781-9796.